nuclear fusion
IAEA

PAPER • OPEN ACCESS

Pedestal main ion particle transport inference through gas puff modulation with experimental source measurements

To cite this article: A.M. Rosenthal *et al* 2024 *Nucl. Fusion* **64** 036006

View the article online for updates and enhancements.

You may also like

- Overview of density pedestal structure: role of fueling versus transport
S. Mordijck
- Direct gyrokinetic comparison of pedestal transport in JET with carbon and ITER-like walls
D.R. Hatch, M. Kotschenreuther, S.M. Mahajan et al.
- The dependence of exhaust power components on edge gradients in JET-C and JET-ILW H-mode plasmas
A R Field, C D Challis, J M Fontdecaba et al.

This content was downloaded from IP address 198.124.216.150 on 25/06/2024 at 18:21

OPEN ACCESS
IOP Publishing | International Atomic Energy Agency
Nuclear Fusion
Nucl. Fusion **64** (2024) 036006 (11pp)
https://doi.org/10.1088/1741-4326/ad17f5

Pedestal main ion particle transport inference through gas puff modulation with experimental source measurements

A.M. Rosenthal[1,*], J.W. Hughes[1], F.M. Laggner[2], T. Odstrčil[3], A. Bortolon[4], T.M. Wilks[1], S. Mordijck[5], M.A. Miller[1] and F. Sciortino[6]

[1] Plasma Science and Fusion Center, Massachusetts Institute of Technology, 175 Albany Street, Cambridge, MA 02139, United States of America
[2] Department of Nuclear Engineering, North Carolina State University, Raleigh, NC 27607, United States of America
[3] General Atomics, San Diego, CA 92186-5608, United States of America
[4] Princeton Plasma Physics Laboratory, Princeton, NJ 08543, United States of America
[5] William & Mary, Williamsburg, VA 23185, United States of America
[6] Max-Planck-Institute of Plasma Physics, Boltzmannstraße 2, Garching, Bayern 85748, Germany

E-mail: aaronmr@mit.edu

Received 24 October 2023
Accepted for publication 21 December 2023
Published 24 January 2024

Abstract

Transport in the DIII-D high confinement mode (H-mode) pedestal is investigated through a periodic edge gas puff modulation (GPM) which perturbs the deuterium density and source profiles. By using absolutely calibrated experimental edge ionization profile measurements, radial profiles of diffusion (D) and convection (v) are calculated into the pedestal region without depending on modeling the edge ionization source. An analytic approach with closed-form expressions for the D and v profiles and a more advanced Bayesian approach show evidence of an inward particle convection on the order of 1 m s^{-1} extending to normalized poloidal flux (Ψ_N) of 0.98. Meanwhile, diffusion reaches a minimum value of (0.03 ± 0.02) m^2 s^{-1} in the pedestal region. Notably, the Bayesian approach, which utilizes the Aurora 1.5 D forward model inside the IMPRAD OMFIT module, provides radially resolved transport profiles with associated uncertainty without requiring an explicit form for the perturbation to the density profile or source. The combination of experimental ionization measurements and Bayesian inference provides an enhanced robust framework for investigating edge particle transport coefficients to experimentally test transport physics in order to improve predictive capabilities in the tokamak edge.

Keywords: plasma, pedestal, fueling, transport

(Some figures may appear in colour only in the online journal)

* Author to whom any correspondence should be addressed.

Original Content from this work may be used under the terms of the Creative Commons Attribution 4.0 licence. Any further distribution of this work must maintain attribution to the author(s) and the title of the work, journal citation and DOI.

© 2024 The Author(s). Published by IOP Publishing Ltd on behalf of the IAEA. All rights reserved

1. Introduction

Future burning plasma tokamak devices, such as SPARC [1] and ITER [2], are planned to operate in regimes with edge transport barriers. This narrow region, called the pedestal, just inside the last closed flux surface (LCFS) in high confinement mode (H-mode), is characterized by steep gradients in both density and temperature and boosts the overall plasma performance. However, predictive capabilities for the edge density pedestal remain limited, introducing uncertainty into models of future devices. Understanding the transport in the pedestal region is a critical gap in predicting current and future devices [3, 4].

Predicting the edge pedestal remains challenging due to complex interactions between atomic and transport physics. In the edge region, ionization of neutral particles causes sources and sinks in multiple channels such as momentum, density, and radiation. The continuity equation,

$$\frac{\partial n}{\partial t} = -\nabla \cdot \Gamma + S \tag{1}$$

and diffusive-convective ansatz

$$\Gamma = -D\nabla n + vn \tag{2}$$

provide an experimentally testable model of the particle transport which forms the density pedestal. Here n is the density, Γ is the flux, S is the particle source, D is the diffusive coefficient, and v is the convective coefficient. In previous studies of stationary plasmas, equation (2) is under-determined, so edge transport can only be described with a single transport coefficient [5–7]. However, examining dynamic events allows the more detailed description of transport with diffusion (D) and convection (v) coefficients. Multiple techniques have been developed to probe the individual contributions of D and v studying the Edge Localized Mode (ELM) rebuild [8, 9], L to H transition [10], pellet injection, and modulation of the heating source among others. A particularly adaptable technique has been gas puff modulation (GPM), where a periodic perturbation is applied by an edge gas valve to modulate the density profile.

GPM experiments have been conducted in the core and edge of fusion plasmas in tokamaks and stellerators [11–20]. In the edge or pedestal region, the particle source is non-negligible. Previous GPM experiments in this region relied on time-independent modeling of edge ionization source profile using 1.5-dimensional codes [19, 20]. However, since experimental edge source measurements were unavailable, the edge source modeling was not experimentally validated. Additionally, modulation of the edge source by GPM was not captured in time-independent models. As a result, analysis techniques and conclusions from experiments without experimental edge source measurements are limited by the fidelity of edge modeling.

In this work, a method for GPM experiments in the pedestal region is developed on the DIII-D tokamak utilizing an experimental measurement of the time-dependent main ion edge ionization source profile. The **L**LAMA is the **L**yman-**A**lpha **M**easurement **A**pparatus (LLAMA) diagnostic provides a one-dimensional absolutely calibrated measurement of the hydrogenic Lyman-alpha (Ly-α) brightness which can be used to infer the local ionization source through rate coefficients [21–23]. Experimental determination of the ionization source facilitates analytic and advanced Bayesian inference of the transport coefficients. In the analytic approach, density and ionization profiles are fit with sinusoidal functions allowing evaluation of closed-form expressions of D and v from the perturbation amplitudes and phases. In the Bayesian inference approach, the 1.5D forward model Aurora inside the IMPRAD framework [24] is utilized to infer particle transport coefficients without prescribing forms to the density and source perturbation. Furthermore, the forward model captures both the steady state and perturbed density profiles. The two approaches are applied and compared on a high confinement mode (H-mode) discharge on the DIII-D tokamak to provide the first experimental test of particle transport using GPM in the pedestal region with experimental ionization source measurements.

2. Experimental technique and shot description

In GPM experiments, a periodic waveform is applied to perturb the source and density. The difficulty in GPM experiments is finding a sufficient gas puff to modulate the density at a detectable level without applying a modulation that substantially changes the underlying transport. In order to minimize the effect of the gas puff on the underlying transport, multiple shots were utilized to develop the gas waveform so as not to significantly change the underlying density profile and use the minimum gas flow rate necessary to provide a measurable perturbation.

An overview of the studied lower single null (LSN) H-mode discharge is shown in figure 1. The plasma shape, shown in figure 1(a), was selected for its good diagnostic coverage of the pedestal region to constrain the ionization rate and main ion density. The high field side (HFS) and low field side (LFS) LLAMA system [21] provides views about the pedestal in the lower chamber giving absolutely calibrated profiles [22] of the main ion ionization source. Meanwhile, the Thomson Scattering (TS) [25], reflectometer [26], CO_2 interferometer [27], and Charge-exchange Recombination Spectroscopy (CER) system [28] are used to constrain the main ion density. The magnetic field, B, is 2 T with $B \times \nabla B$ pointed towards the active x-point. A plasma current of 1.0 MA was selected to achieve a density pedestal with a modest pedestal top value of approximately 5×10^{19} m^{-3}. A constant 3.5 MW Neutral Beam Injection (NBI) heating is applied throughout the shot. The Z_{eff} as measured by the CER system [28] is approximately constant at 2, with a single radial location shown in figure 1(e).

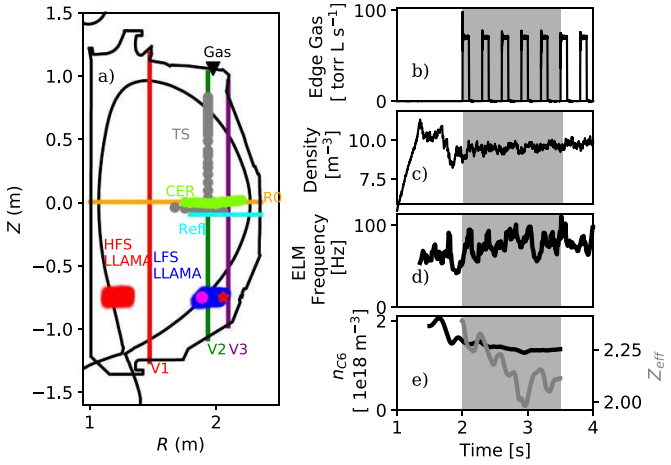

Figure 1. Overview of discharge 189109 and diagnostics utilized to constrain main ion density. (*a*) Poloidal cross-section of the DIII-D tokamak highlighting the last closed flux surface (LCFS) for the studied discharge. The LLAMA views are shown for the inboard (red) and outboard (blue) view. The CO_2 interferometer chords (red, green, purple and orange), Thomson Scattering (TS) views (grey) reflectometry (cyan) and Charge-exchange Recombination Spectroscopy (CER) (light green) are utilized to constrain the main ion density. Gas was injected from two valves near the crown of the plasma indicated by a black triangle. Time traces of the (*b*) periodic injected gas waveform, (*c*) line average density from the V3 interferometer chord, and (*d*) average ELM frequency from an edge filterscope channel. The analysis window is highlighted in grey. (*d*) Fully stripped carbon density and Z_{eff} at normalized poloidal flux (Ψ_N) of 0.9. Fully stripped carbon shows no coherent modulation with the gas puff.

A deuterium edge gas puff is applied from the scrape-off layer (SOL) by a fast piezo valve near the outboard side of the crown, whose location and waveform are shown in figures 1(*a*) and (b). The crown valve was utilized to avoid directly injecting gas into the views of the LLAMA system which could complicate the data analysis procedure. The resulting line average density is shown in figure 1(*c*), and Balmer-alpha (B-α) filterscope response used to identify ELMs is shown in figure 1(*d*). The observed ELM frequency is approximately equal to that of matched discharges without GPM. The grey region indicates the time period studied. The relatively low pedestal top density compared to typical high current discharges allows external modulation with smaller rates of gas injection. The gas valve period is targeted to be below the particle confinement time [29]. The high ELM frequency, of about 80 Hz, is best probed by a low frequency GPM, allowing the GPM to probe ELM-cycle averaged transport coefficients. As a result, the modulation frequency was chosen to be about a factor of 10 smaller than the 80 Hz ELM frequency. The amplitude of the gas puff was determined by trial and error, balancing the desire for a measurable perturbation without significantly increasing the line average density. The resulting best-performing gas injection waveform had an amplitude of 2×10^{21} molecules s^{-1}, with an open valve time of 100 ms, and a closed time of 200 ms. As evidenced in figure 1(*d*), the ELM frequency during periods with and without injected gas varies by less than 20%. While the electron density varies by about 10% in the pedestal.

3. Analytic analysis of transport coefficients from GPM

For the analytic approach, it is assumed that both the density and phase are perturbed sinusoidally with a linear non-perturbative component. A closed-form expression for the D and v coefficients can be derived from the perturbation form along with the continuity equation and diffusive-convective ansatz. Since the perturbation comes from an edge gas puff, the modulation is first observed in the ionization which then alters the density profile. Towards the core of the plasma, the phase of the density perturbation increases due to the finite time it takes for the perturbation to propagate to the core. Evaluating the D and v profile requires evaluating the spatially resolved phases and amplitudes of the density and source perturbation.

The closed-form expressions for v and D are derived from the purely radial continuity equation and diffusive convective ansatz

$$\frac{\partial n}{\partial t} = -\frac{1}{r}\frac{\partial}{\partial r}(r\Gamma) + S \tag{3}$$

$$\Gamma = -D\frac{\partial n}{\partial r} + vn \tag{4}$$

The radial coordinate utilized is a plasma volume, V, weighted coordinate given by

$$r_V = \sqrt{\frac{V}{2\pi^2 R_{\text{axis}}}} \tag{5}$$

which maps the flux surface volumes to a 1D cylindrical geometry using the magnetic axis, R_{axis} as the center of the cylinder. In comparison to previous GPM [17, 18], r_V includes the 2D flux geometry while still using the simple radial expressions evaluated in cylindrical geometry for the continuity and diffusive-convective ansatz. This effectively makes the D and v quantities flux-surface averaged. It is possible to compare the results of the v and D profiles to previous studies which measure a local poloidally dependent coefficient by including a geometrical correction factor [30].

The closed-form expressions for v and D are derived by assuming that the perturbation to the source, S_{pert} and the density, n_{pert}, takes the form of a complex sinusoid

$$S_{\text{pert}} = A_s(r)\, e^{i(\omega t + \phi_s(r))} \tag{6}$$

$$n_{\text{pert}} = A(r)\, e^{i(\omega t + \phi(r))} \tag{7}$$

where ω is the angular frequency of the perturbation and t is time. Both the source and density have radially dependent perturbation amplitudes and phases. The source perturbation amplitude, A_s, and phase, ϕ_s, are indicated with a subscript s, while the density amplitude and phase have no subscript.

Plugging equations (6) and (7) into the radial continuity (3) and diffusive-convective ansatz (4). The resulting expression for the D coefficient is

$$D(r) = \frac{-\omega X(r)}{r\frac{\partial\phi}{\partial r}A(r)}. \tag{8}$$

For the convection coefficient, the expression is given by

$$v(r) = \frac{\omega Y(r)A(r)}{r} + D(r)\frac{\partial A}{\partial r}. \tag{9}$$

The variables X and Y, which are also functions of the radial coordinate, are given by

$$X(r) = \int_0^r \left[A(r')\cos(\phi(r') - \phi(r)) + \frac{A_s(r')}{\omega}\sin(\phi_s(r') - \phi(r))\right] r'\mathrm{d}r' \tag{10}$$

$$Y(r) = \int_0^r \left[-A(r')\sin(\phi(r') - \phi(r)) + \frac{A_s(r')}{\omega}\cos(\phi_s(r') - \phi(r))\right] r'\mathrm{d}r'. \tag{11}$$

The derived expressions depend solely on the amplitude and phase of the perturbation not requiring any consideration of the steady-state fueling from either the edge or neutral beams. Furthermore, the gas puff phase is not relevant to evaluating the expressions. However, these equations do have some limitations and assumptions:

(i) D and v depend on the derivative of the phase in the denominator which can be very sensitive to noise particularly where the phase changes slowly with radius.
(ii) The flux is assumed to be linearly related to the gradients and absolute values of the density.
(iii) Transport coefficients are assumed to be time-independent and ELM averaged.
(iv) Transport is assumed to be purely radial (perpendicular to the B-field lines) which is likely insufficient in the SOL [31, 32].
(v) Any poloidal dependence is flux surface averaged creating the 1.5D geometry.

Evaluating the phase and amplitude of the ionization source is achieved utilizing the LLAMA measurements. The procedure for converting the local line integrated brightness measurement to the ionization rate, shown for the LFS in figure 2, is described in a previous paper [8]. A few unique signal processing steps are applied for identifying sinusoidal modulation. By using an edge filterscope channel to identify the ELMs, only Ly-α brightness data from 20 to 98 percent of the ELM cycle is included. The brightness data is further filtered by a Savitzky–Golay filter [33] at one-quarter the modulation frequency to smooth-over higher frequency signals. The data is then inverted to calculate the local emissivity and combined with density and temperature measurements to calculate the ionization rate shown in figure 2(c). The ionization is near sinusoidal with a modest linear slope, which is removed before extracting the amplitude and phase.

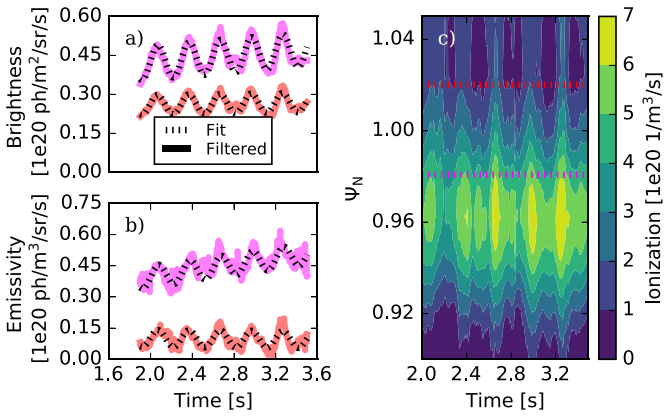

Figure 2. The injected gas waveform form results in a near sinusoidal perturbation to the deuterium source measurements from LLAMA. (a) Unfiltered brightness from two LFS LLAMA channels indicated by the circle and star in figure 1(a) along with least-square complex sinusoidal fits to the brightness data. (b) Fits of the emissivity were calculated by inverting the line-integrated brightness measurements from the same radial location. (c) Ionization as a function of time and normalized poloidal flux (Ψ_N). The radial locations highlighted in figures (a) and (b) are indicated by the horizontal lines.

The density profiles and perturbation are determined from a 2D Gaussian Process Regression (GPR) fitting algorithm [34] which simultaneously provides fits in flux-coordinate space and time. A 3D plot of the resulting electron density fit and a temporal plot at normalized poloidal flux (Ψ_N) of 0.7, 0.85, and 0.96 is highlighted in figures 3(a) and (b). Figure 3(c) shows the average density profile from the same window for comparison. The 2D fits were created using temporal smoothing parameters selected to extract the 300 ms periodic modulation. The CO_2 interferometer and TS system are utilized to constrain the electron density fit. The TS measurements are scaled such that the line average density inferred from the TS matches that of the CO_2 interferometer. Although their effect is minimal after temporal smoothing, ELMs are excluded before smoothing using a photodiode channel to identify the ELM onset and end resulting in the exclusion of a few milliseconds of data during the ELM event. The time-dependent evolution of the ELM is then inferred from all data outside of this brief window. Exclusion of the ELM data makes the focus of this analysis on the intra-elm transport. To align the density profiles with the separatrix, a stretch of the density and temperature profiles is required to account for the inaccuracy in the magnetic reconstruction. The separatrix temperature is determined using a two-point model [35] as in [36] without considering the flux-limited heat flux term. The scrape-off layer power fall-off length, λ_q is calculated using the Eich scaling [37] with the separatrix temperature given by

$$T_{e,sep} = \left(\frac{7}{16}\frac{L_{||}P_{SOL}|B|}{\pi R\kappa_0 B_p \lambda_q}\right)^{2/7} \tag{12}$$

where P_{SOL} is the power flowing across the separatrix into the SOL, $|B|$ is the midplane total magnetic field, B_p is the poloidal magnetic field at the midplane, R is the major radius,

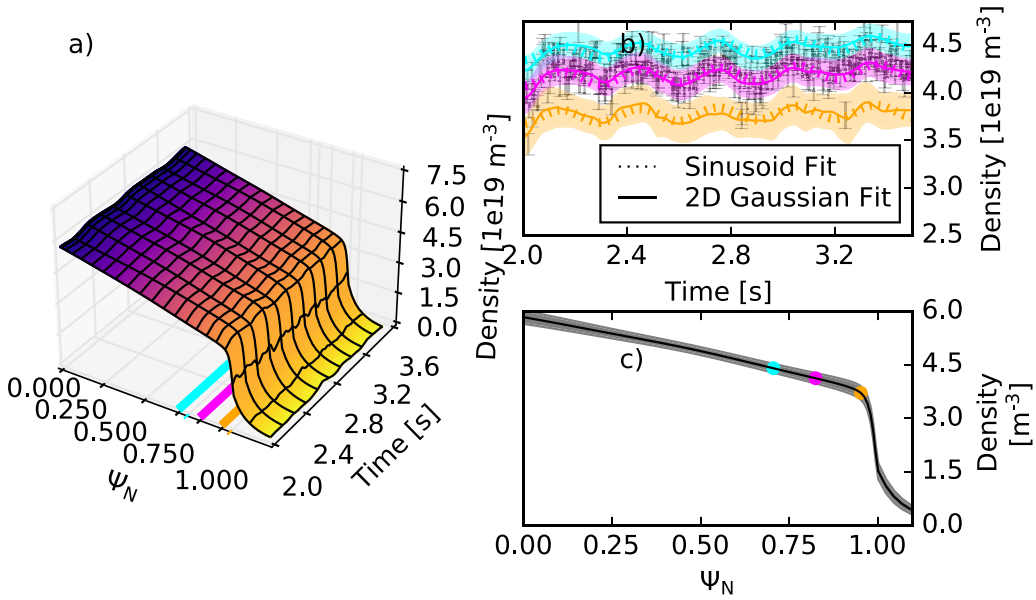

Figure 3. Resulting modulation in the electron density (*a*) simultaneous fitting in space and time of electron density measurements from the CO_2 interferometer and TS systems, highlighting the radial and temporal modulation. (*b*) Modulation at a selection of radial locations from the 2D Gaussian Process Regression (GPR) fitting algorithm along with complex sinusoidal fits to the underlying data. For comparison, the TS data for a single channel is shown in black. (*c*) ELM-synchronized average density profile from the time period studied. The radial location of the temporal data is shown in figures (*a*) and (*c*) by the cyan, magenta, and orange lines.

$L_{||}$ is the parallel connection length from the midplane to the target and κ_0 is the electron heat conduction coefficient as defined in equation 4 of [38]. The electron temperature profile is stretched such that the temperature at the LCFS matches the temperature calculated by the two-point model. This is achieved by dividing the radial coordinate by the location of the temperature found by the two-point model and then linearly interpolating onto that new coordinate. The density profiles are stretched by the same factor. Figure 3 shows a near sinusoidal behavior in the fit density profile with increasing phase (or delay) towards the core. The electron density typically does not equal the main ion density due to the presence of impurities. On DIII-D, due to the carbon wall, carbon is the dominant impurity. Although there is some evolution, the carbon impurity source is not coherently modulated by the gas puff as shown in figure 1(*e*). Therefore, it is assumed that the electron density perturbation equals the main ion density perturbation. On DIII-D, the main-ion density can be calculated from Main Ion Charge-exchange Recombination (MICER) [39]; however it was unavailable for GPM discharges which included LLAMA data.

The resulting phase and amplitude profiles for both the source and density are shown in figure 4. The phase is reported in seconds with zero representing the phase inferred from the complex sinusoidal fit to the edge gas puff show in figure 1(*b*). Error bars for the density perturbation come from a Monte Carlo approach. For the density, the TS and CO_2 interferometer data points are perturbed within their error bars; the data is then refitted using the 2D GPR algorithm. Each fit is then analyzed for the amplitude and phase of the perturbation. A Gaussian distribution is fit to the inferred amplitude and phases from all density profiles with the resulting displayed error bars representing one standard deviation of the normal distribution. Error bars in the ionization are estimated from the fits to the ionization, inversion error, and absolute calibration error. The source phase is approximately constant, while the density phase increases rapidly in the pedestal and more slowly inside the pedestal. Meanwhile, the amplitude of perturbation in the source and density falls off after peaking near the LCFS.

Profiles of D and v calculated from the amplitude and phase are shown in black in figure 5. The error, shown by the shaded grey region, is calculated by a Monte Carlo approach as described for the density amplitude and phase measurements. The uncertainty in both D and v becomes large between Ψ_N of 0.85 and 0.9 due to the decreasing perturbation amplitude and the derivative of the phase in the denominator in equation (8). In this region, the phase is slowly changing, near zero, dominating the uncertainty. An inward pinch of approximately $(1 \pm 2)\,\mathrm{m\,s^{-1}}$ extends to Ψ_N of 0.98. In the pedestal, the diffusion has a minimum on the order of 0.01 $\mathrm{m^2\,s^{-1}}$. Two counterfactuals are also plotted in figure 5 to emphasize the importance of the experimental source measurement. The magenta solid lines are calculated using the experimental amplitude measurement from LLAMA (figure 4(*d*)) and artificially setting the source phase ($\phi_s(r)$ in equations (8)–(11)) to zero, implying instantaneous modulation with the gas-valve, as has been done in previous work [19]. In dash-dotted magenta, the source amplitude ($A_s(r)$ in equations (8)–(11)) is artificially set to zero, while the phase is calculated from the experimental data shown in figure 4(*c*). In the pedestal region, from Ψ_N of $\sim$ 0.95 to 1.0, these two results span over an order of magnitude in diffusion and can change the sign of the convection near the LCFS.

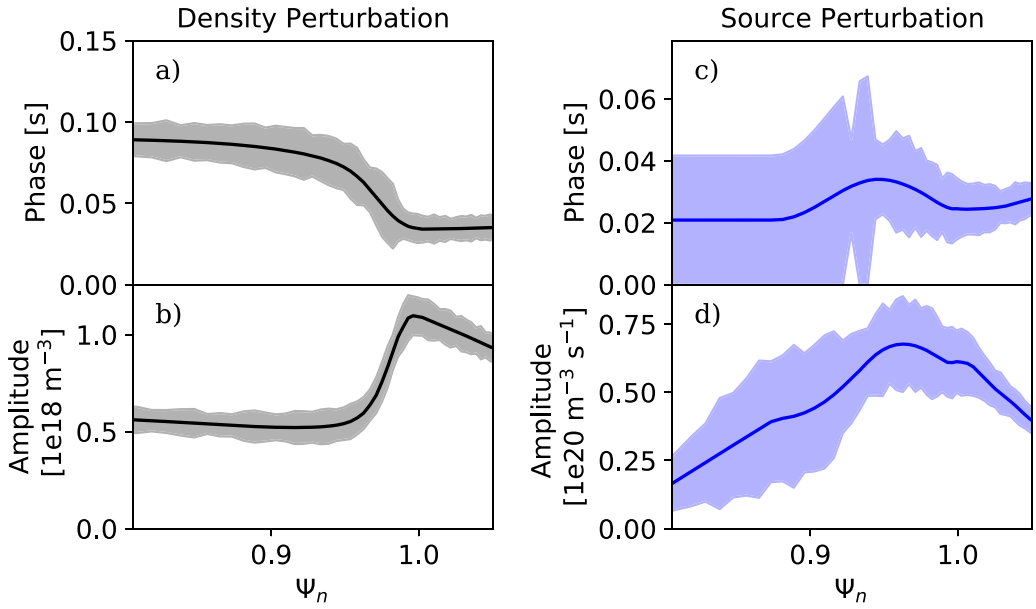

Figure 4. Measured perturbations from the sinusoidal fits for the (*a*) density phase, (*b*) density amplitude, (*c*) source phase, and (*d*) source amplitude. The source perturbations come from the LFS LLAMA system.

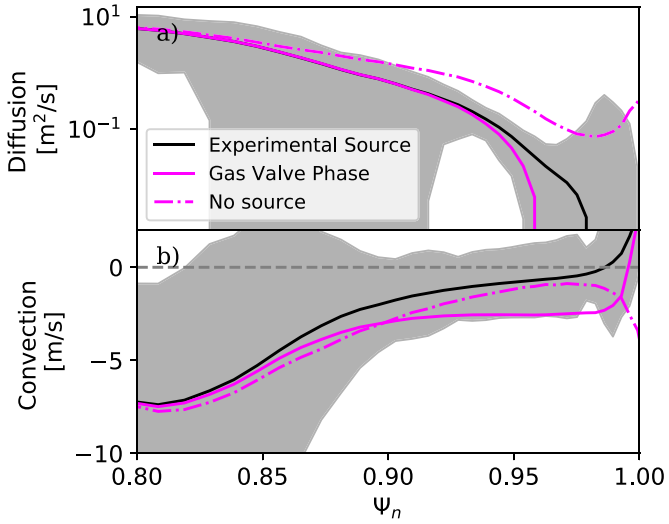

Figure 5. In black, H-mode (*a*) diffusion (*b*) and convection coefficient profile using the experimental source measurement with the analytic approach. In the pedestal region, the diffusion coefficient reaches a minima of 1×10^{-2} m^2 s^{-1} and the convection coefficients has a small inward (negative) value until Ψ_N of 0.98. Two counterfactuals are plotted in magenta to emphasize the importance of the experimental source measurement. The source amplitude is set to zero resulting in the dash-dot magenta line. Similarly, the phase was artificially set to zero, implying simultaneous modulation with the gas valve, in the solid magenta profiles.

While the analytic approach for inferring main ion transport coefficients successfully provides physical profiles of the v and D profiles during GPM experiments, error bars remain large due to the sensitivity of the closed-form expressions to derivatives. It should also be emphasized that the fitting parameters in the density can affect the inferred transport coefficients. Furthermore, the closed-form expressions for D and v require sinusoidal behavior which can be challenging to achieve experimentally. Forward modeling approaches of transport coefficient inference remove the need for prescribed perturbation forms and opens the possibility of modeling more advanced perturbations.

4. Forward modeling for transport coefficient inference

The Aurora forward model coupled to Bayesian inference in the IMPRAD [40, 41] OMFIT [42] module offers a more advanced method of transport coefficient inference. Aurora is a 1.5D transport code originally developed for impurity transport which has been adapted for main ion transport studies with the addition of more explicit inclusion of the ionization source. The transport model in Aurora utilizes the same equations specified in equations (3)–(5) with the addition of a simple 0D SOL and divertor model. The Aurora and IMPRAD framework does not require fitting the main ion density profiles, directly calculating derivatives, or prescribing sinusoidal forms for the perturbation. Instead, the forward model of the main ion density is directly compared through a synthetic diagnostic, which has recently been added to the code for electron density diagnostics, to the experimental density measurements. Bayesian inference compares the forward model results to the experimental data determining the D and v profiles which most closely match the experimental data. For the IMPRAD inference, the analytic result is used as the Bayesian prior, and forward modeling shows results that are consistent with the analytic approach.

The Aurora forward model uses the time-dependent main ion source, initial main ion density, magnetic geometry, and plasma profiles as inputs. The plasma profiles from the 2D fit from the GPR [34] shown for the density in figure 3 are

Table 1. Summary of initial parameters, number of free parameters (NFP), and distributions for Bayesian Inference in IMPRAD for discharge 189109. For example, the fourth D knot (one of the 5 free parameters for D), highlighted in yellow in the table, is assumed to have a truncated Gaussian distribution whose mean value is 0.02, truncated at 10^{-3} on the low-end and 10^{2} on the high end. The knot associated with that D is from a constant distribution from Ψ_N of 0 to 1.1 initially located at Ψ_N of 0.99.

Quantity	NFP	Distribution	Parameter	Value				
D	5	Truncated	Mean	0.25	1.4	6.0	0.02	0.2
[$m^2\ s^{-1}$]		Gaussian	Min–Max	0.01–100			10^{-3}–10^{2}	0.01–100
D knots	5	Constant	Initial	0.2	0.5	0.94	0.99	1.1
[ρ_p]			Range	0–1.1				
v	5	Gaussian	Mean	−0.2	−3.0	−6.0	−0.2	1.0
[$m\ s^{-1}$]			Sigma	2.5	2.5	50	100	100
v knots	5	Constant	Initial	0.4	0.8	0.93	0.99	1.1
[ρ_p]			Range	0–1.1				
SOL	1	Log	Initial	0.05				
Mach #		Uniform	Min–Max	0.01–0.2				

used to generate time-independent rate coefficients. The initial main ion density is assumed to be equal to the initial electron density scaled by a radially uniform dilution factor of 0.8. The dilution factor is calculated from the Z_{eff} and by assuming that carbon, from the walls of DIII-D, is the sole impurity. Since few experimental constraints exist on the radial density profiles of non-fully stripped carbon, a radially uniform dilution factor is assumed from the fully stripped carbon density profile measured by the CER system [28]. The main ion source is taken from the LFS LLAMA system shown in figure 2(*c*) along with a steady-state NBI source profile calculated from NUBEAM [43]. Geometric edge parameters that inform the 0D SOL model are pulled from a representative EFIT time slice from the discharge.

IMPRAD iteratively runs Aurora, altering the D and v profiles, comparing the modeled main ion density evolution through synthetic diagnostics to experimental data to determine the transport coefficient profiles which most closely recreate the experimental behavior [24]. Direct measurement of the main ion density was not available on this discharge. Therefore, the electron density measurements by the CO_2 interferometer, TS, and reflectometer systems are used to infer the main ion density. [25, 26, 44]. Since carbon makes a non-negligible contribution to the steady-state electron density measurement, the main ion density is calculated by taking the temporal average of the density diagnostics, scaled by the radially uniform dilution factor of 0.8 and adding on the perturbation to the electron density. A radial shift is applied to the Aurora simulations to align the pedestals with the reflectometer and TS data due to uncertainty in the separatrix location. Due to the high scatter in raw TS points, the TS system is weighted half as much in the Bayesian framework as the reflectometry and interferometry systems which can more clearly resolve a spatially varying phase and amplitude of the perturbation. The TS system does not supply a strong constraint on the phase and amplitude of the perturbation without the fitting of the TS data, which is not performed in the IMPRAD framework. However, the TS system is still included in the inference as it constrains the overall radial density profile.

The analytic results derived in section 3 are used as the means for the Bayesian priors for running the Bayesian inference using the Aurora forward model. Table 1, describes the means and distributions used for the Bayesian Inference. While the analytic approach provides a good estimate for the initial or mean parameter for the Bayesian inference, the model is given significant freedom in regions where a wide range of D or v coefficients are feasible, making the inference less sensitive to the initial or mean parameter. For example, for the fourth diffusion knot, highlighted in yellow, the Gaussian distribution spans from $1 \times 10^{-3}\ m^2\ s^{-1}$ to $1 \times 10^{2}\ m^2\ s^{-1}$. Although more advanced methods exist [40], the number of free parameters is chosen by individually adding spline knots for D and v coefficients until the experimental data can be captured by the model. Five spline knots for both the diffusion and convection profiles were the minimum free parameters necessary to begin capturing the steady state and perturbation behavior. The inference varies the positioning of the spline knots while maintaining their relative ordering to each other. In total, there are 21 free parameters for the Bayesian inference.

Bayesian inference is run using the Levenberg–Marquardt minimization method [45, 46] inside the IMPRAD framework resulting in the inferred transport coefficients shown in red in figures 6(*a*) and (*b*). The analytic solution is overplotted in the blue dotted line for comparison. Aurora synthetic diagnostics are overlayed with the scaled electron density diagnostic traces from the CO_2 interferometer and reflectometer in figures 6(*c*) and (*d*). The modulation is well captured in the four lines of sight of the interferometry system shown in figure 6(*c*). The radial decay in the phase of the modulation in the reflectometry diagnostic, shown in figure 6(*d*), is well captured by the diagnostic with some disagreement in amplitude particularly

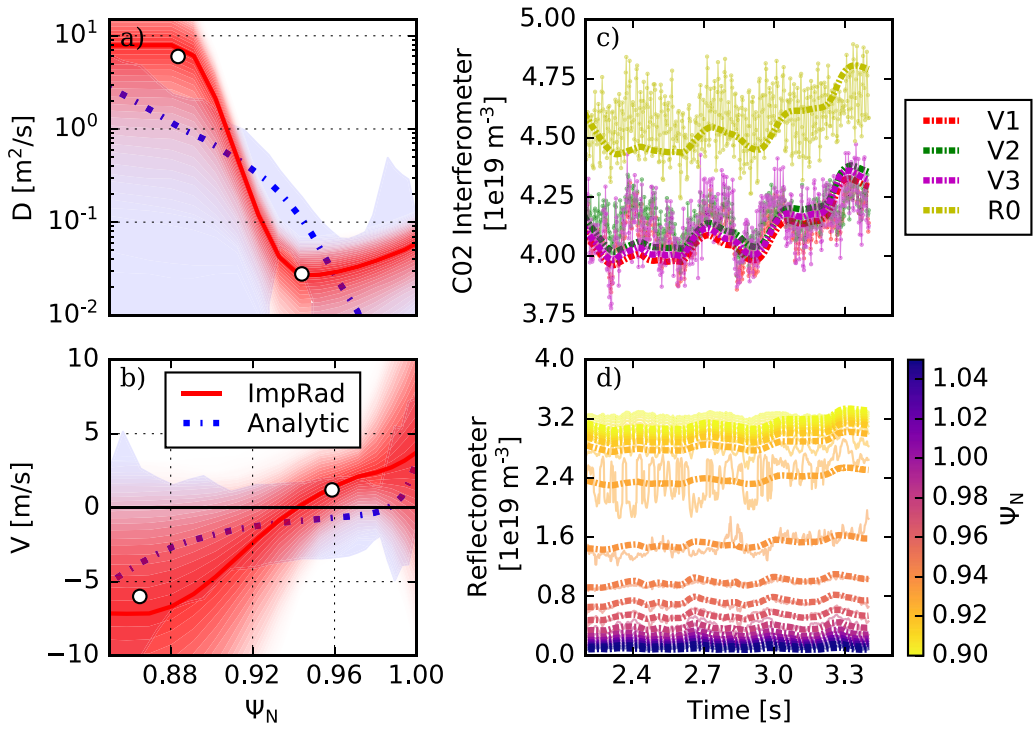

Figure 6. (a) Diffusion and (*b*) convection profiles from IMPRAD inference using the Aurora forward model in red along with the analytic approach in blue. The spline knots are indicated in white. The best result of the forward model inference is compared to the experimental (*c*) CO_2 interferometer chords and (*d*) reflectometer. The forward model synthetic diagnostics results are shown by the dashed lines. The colors for the CO_2 interferometer sight-lines match those in figure 1(*a*).

towards the core due to differences in the TS, CO_2 interferometer and reflectometer measured amplitude of perturbation. Overall, the χ^2/degree-of-freedom is 1.4 for the best-fitting result indicating a slight underfitting of the experimental data.

5. Discussion and conclusion

Both the analytic approach and the IMPRAD result infer D and v profiles with a diffusion in the pedestal on the order of 0.05 m s^{-2} and an inward convection on the order of 1 m s^{-1} which becomes outward between Ψ_N of 0.95 to 0.97. The results from the analytic approach capture similar order of magnitude results but have slightly different radial profiles, including a slightly different radial location where the v switches from inward to outward. While the two convection profiles show significant overlap inside their error-bars, more accurately locating the radial extent of inward convection, which will require a reduction in uncertainty, is important to physically understanding the processes forming the density pedestal. The difference in the inferred transport coefficients between the two methods is the result of a number of distinctions in the two analyses. In the IMPRAD approach, the steady state profile is modeled simultaneously with the perturbation. Meanwhile, the analytic approach solely considers the perturbation which can lead to differences in the measured perturbed coefficients with the underlying coefficients [18, 29]. Furthermore, the analytic approach requires the sinusoidal perturbation form and spatial smoothing in the 2D GPR used for the density perturbation.

Both the analytic and IMPRAD approach do not account for poloidal asymmetries in the density or source. In particular, the source is expected to have a significant poloidal asymmetry as observed on previous shots [8] and suggested in simulation of other shots on DIII-D [47–49]. In this discharge, only the LFS LLAMA source is utilized for transport inference as the modulation is clearer than the HFS and more investigation is required to determine how to provide a poloidal average of the two views. Furthermore, the main ion density which is inferred from the uniform radial dilution factor by carbon could inaccurately determine the main ion density. This could be particularly true in the pedestal where multiple, possibly poloidally asymmetric, carbon charge states may be present. Both of these simplifications, introduce uncertainty in the inferred transport coefficients which is not reflected in the error bars shown in figures 6(*a*) and (*b*).

In both methods of analysis, a few milliseconds of data of the ionization and electron density are not included whenever an ELM occurs. The exclusion of this data as well as the smoothing parameters that focus on the slow modulation, limit the measurement of the D and v coefficients to the inter-ELM transport. The v and D profiles do not provide a measurement of the fast filamentary transport that occurs during an ELM. Furthermore, the exclusion of data during an ELM may introduce uncertainty in the time derivative term in equation (3) which is not accurately reflected in the v and D profiles. However, the techniques utilized here could easily be

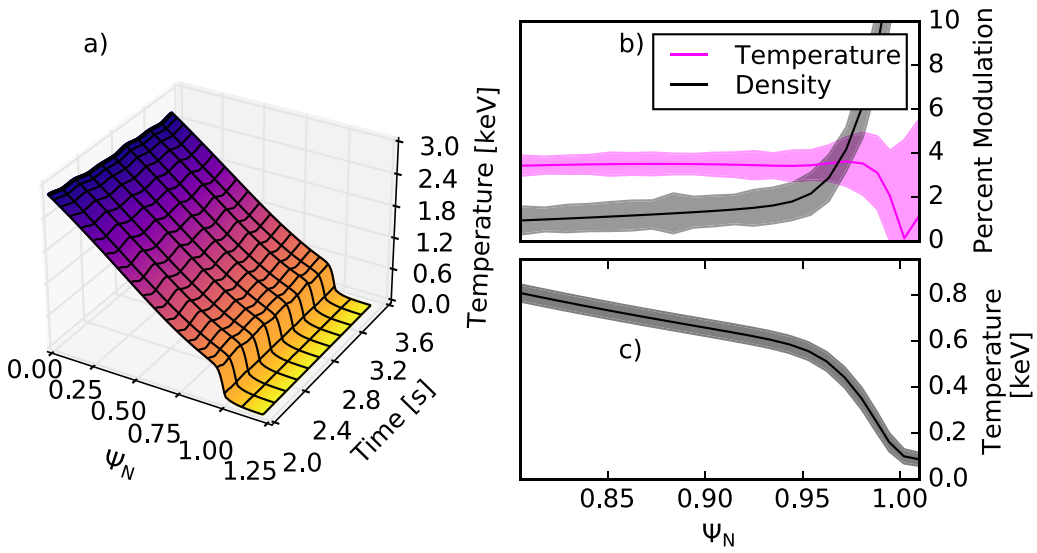

Figure 7. (a) 2D GPR fit to the electron temperature profile (*b*) comparison of percent modulation, calculated by dividing the amplitude of perturbation by the mean profile, in temperature (magenta) and density (black). Density modulation dominates in the pedestal region. (*b*) ELM-synchronized mean temperature profile from the same time period.

applied to ELM free regimes such as low-confinement mode (L-mode) or intermediate confinement mode (I-mode) [50]. Furthermore, in principle, the techniques here could also be used to study the transport during an ELM if both ionization and density data were available at sufficient temporal resolution. Although, ultimately a diffusive-convective ansatz may prove insufficient to describe such behavior.

Compared to previous investigations of pedestal transport in the pedestal region without experimental measurements of the particle source, the v coefficient order of magnitude is broadly consistent [51] while the D is consistent with H-mode studies and an order of magnitude smaller than the D coefficient found in L-mode studies. In ASDEX-U (AUG) L-mode discharges, the time-independent convection coefficient was best represented by $(-1 \pm 2)\,\mathrm{m\,s^{-1}}$ with a D of $(0.20 \pm 0.13)\,\mathrm{m^2\,s^{-1}}$ [20]. Examination of the H-mode after an L to H transition on AUG found a D of $0.03\ \mathrm{m^2\,s^{-1}}$ and v of -0.5 to $5\ \mathrm{m\,s^{-1}}$ [10]. Work on JET, which did not include a v coefficient found an H-mode D coefficient on the order of $0.05\ \mathrm{m^2\,s^{-1}}$ [52]. Interpretive modeling of the density profile rebuild after an ELM on DIII-D found D coefficient profiles of similar shape and magnitude [53]. Meanwhile, previous work on DIII-D, albeit at a different current, which included the experimental ionization source, shows similar orders of magnitude for inferred transport coefficients, including the v coefficient, [8] with a wider radial extent of the diffusion well in the discharge studied here.

Both the analytic approach and forward modeling approach are able to capture the experimental data without time-dependent transport coefficients. Previous work using the same methods in this paper examining the average rebuild after an ELM in DIII-D [8], GPM experiments from AUG using modeled edge ionization source [20], and strike-point sweep modulation experiments in JET [54] have found evidence for time-dependent transport coefficients. In this experiment, a great deal of care and multiple discharges were utilized to avoid changing the transport coefficients. The edge gas puff programming was designed to limit the effect on the plasma while still providing enough modulation for the analysis. Furthermore, quantities such as $\eta_e = \lambda_{n_e}/\lambda_{T_e}$ where λ_x is the gradient length scale given by $\lambda_x = x/\nabla x$, which have been closely tied to pedestal transport [4, 55, 56], do not evolve significantly during the GPM. While time-independent transport coefficients are utilized to infer the transport coefficients in this discharge, it does not necessarily mean time-independent transport analysis is sufficient for all H-mode GPM experiments. Of particular concern is that GPM does cause a clear modulation in the electron temperature profiles as shown in figure 7(*a*). As gas is injected, the electron temperature drops, possibly leading to changing pedestal transport. However, the modulation in the electron temperature profile is smaller, percentage-wise, than in the electron density profile in the pedestal region, highlighted in figure 7(*b*). Towards the core, the temperature modulation exceeds the density modulation but is overall small percentage wise. The small modulation in both temperature and density likely contributes to the large errorbars reported in the D and v profiles. Finally, there are no un-physical or 'surprising' features in the inferred amplitude and phase behavior shown in figure 4 which have indicated changing transport coefficients in other studies [8, 29, 54]; therefore, time-independent transport coefficients seem sufficient to explain the experimental behavior.

Using the Aurora and IMPRAD framework with experimental ionization source measurements opens a robust and adaptable framework for investigating an increasing number of perturbation experiments to study particle transport. While the resulting D and v is consistent with methods used in other works, the IMPRAD method offers distinct advantages over previous methods including not requiring simulated source profiles, full radial profiles of the transport coefficients, and

uncertainty calculation which was absent from some previous work. The Aurora and IMPRAD framework is capable of capturing complex phenomena such as non-sinusoidal behavior, time-dependent transport coefficients and linear offsets in the density trajectories which previous methods may not be capable of capturing. Furthermore, IMPRAD offers a reduction in uncertainty compared to the analytic approach used in previous studies. While the IMPRAD framework offers a significant advancement in the analysis technique, it should not be mistaken for complexity in execution of the analysis. In the authors experience, implementing analytic approaches requires precision in the execution of an experiment as well as tailored analysis for individual discharges which are not necessarily required in the IMPRAD approach due to its ability to capture more complex physical phenomena.

This work does not comment on scalings for the D and v coefficients or look for experimental signatures of the physical transport process such as turbulent transport or neoclassical transport which underpins those coefficients. Improving the predictive capabilities of the density pedestal will likely require such an understanding and may be only experimentally analyzable using the improved IMPRAD method over previous techniques. Providing experimental tests of transport theories or scalings will likely require a reduction in the error bars of the Bayesian method which can be achieved by further constraining the model with experimental data. Possible valuable additions include the addition of information on the poloidal distribution of the ionization source with increased views or integrated analysis of hydrogenic neutral emission at more poloidal locations. Further attention should also be directed to constraining the main ion density evolution, through direct measurements of the main ion density, ideally achieved on DIII-D with the MICER system [39], or better constraints on the carbon ionization source, or operation in low impurity modes. Finally, it should be experimentally tested that the inferred transport coefficients are unchanged by the GPM programming which would verify that the underlying transport is unchanged by the modulation.

Acknowledgments

A.M.Rosenthal would like to the thank the DIII-D team for their mentorship, time, and effort which facilitated the experiments analyzed in this work.

This material is based upon work supported by the U.S. Department of Energy, Office of Science, Office of Fusion Energy Sciences, using the DIII-D National Fusion Facility, a DOE Office of Science user facility, under Awards DE-SC0014264, DE-AC02-09CH11466, DE-SC0007880, DE-SC0019302 and DE-FC02-04ER54698.

Disclaimer

This report was prepared as an account of work sponsored by an agency of the United States Government. Neither the United States Government nor any agency thereof, nor any of their employees, makes any warranty, express or implied, or assumes any legal liability or responsibility for the accuracy, completeness, or usefulness of any information, apparatus, product, or process disclosed or represents that its use would not infringe privately owned rights. Reference herein to any specific commercial product, process, or service by trade name, trademark, manufacturer, or otherwise does not necessarily constitute or imply its endorsement, recommendation, or favoring by the United States Government or any agency thereof. The views and opinions of authors expressed herein do not necessarily state or reflect those of the United States Government or any agency thereof.

ORCID iDs

A.M. Rosenthal https://orcid.org/0000-0002-6149-1136
J.W. Hughes https://orcid.org/0000-0003-4802-4944
F.M. Laggner https://orcid.org/0000-0003-1601-2973
T. Odstrčil https://orcid.org/0000-0003-4173-4230
A. Bortolon https://orcid.org/0000-0002-0094-0209
T.M. Wilks https://orcid.org/0000-0002-9675-678X
M.A. Miller https://orcid.org/0000-0002-6540-6533
F. Sciortino https://orcid.org/0000-0002-5159-1889

References

[1] Rodriguez-Fernandez P. *et al* 2022 *Nucl. Fusion* **62** 042003
[2] Doyle E.J. *et al* 2007 *Nucl. Fusion* **47** S18
[3] Mordijck S. 2020 *Nucl. Fusion* **60** 082006
[4] Hatch D.R. *et al* 2019 *Nucl. Fusion* **59** 086056
[5] Hughes J.W., LaBombard B., Terry J., Hubbard A. and Lipschultz B. 2007 *Nucl. Fusion* **47** 1057–63
[6] Hughes J.W., LaBombard B., Mossessian D.A., Hubbard A.E., Terry J. and Biewer T. (The Alcator C-Mod Team) 2006 *Phys. Plasmas* **13** 056103
[7] LaBombard B. *et al* (Alcator C-Mod Team) 2008 *Phys. Plasmas* **15** 056106
[8] Rosenthal A.M., Hughes J.W., Laggner F.M., Odstrčil T., Bortolon A., Wilks T.M. and Sciortino F. 2023 *Nucl. Fusion* **63** 042002
[9] Leonard A.W. 2014 *Phys. Plasmas* **21** 090501
[10] Willensdorfer M., Fable E., Wolfrum E., Aho-Mantila L., Aumayr F., Fischer R., Reimold F. and Ryter F. (The ASDEX Upgrade Team) 2013 *Nucl. Fusion* **53** 093020
[11] Gentle K.W., Richards B. and Waelbroeck F. 1987 *Plasma Phys. Control. Fusion* **29** 1077
[12] O'Rourke J., Gowers C., Kramer G.J., Morgan P.D., Simonini R. and Sips A.C.C. 1993 *Plasma Phys. Control. Fusion* **35** 585
[13] Takenaga H., Nagashima K., Sakasai A., Oikawa T. and Fujita T. 1998 *Plasma Phys. Control. Fusion* **40** 183–90
[14] Mordijck S. *et al* 2012 *Phys. Plasmas* **19** 056503
[15] Mordijck S., Rhodes T.L., Zeng L., Doyle E.J., Schmitz L., Chrystal C., Strait T.J. and Moyer R.A. 2015 *Plasma Phys. Control. Fusion* **58** 014003
[16] Mordijck S. *et al* 2015 *Nucl. Fusion* **55** 113025
[17] Salmi A. *et al* 2015 Particle source and edge transport studies in JET H-mode gas puff modulation experiments (Lisbon, Portugal) *42nd European Physical Society Conf. on Plasma Physics* (*Lisbon Portugal*, *22 June 2015*) p 4 (available at: http://www.ipfn.ist.utl.pt/EPS2015/")
[18] Mordijck S. *et al* 2020 *Nucl. Fusion* **60** 066019
[19] Ohtani Y., Tanaka K., Tokuzawa T., Akiyama T., Yamada I., Yasuhara R., Funaba H., Shoji M. and Goto M. (LHD

Experimental Group) 2020 *Plasma Phys. Control. Fusion* **62** 025029
[20] Schuster C.U. *et al* 2022 *Nucl. Fusion* **62** 066035
[21] Rosenthal A.M. *et al* 2021 *Rev. Sci. Instrum.* **92** 033523
[22] Laggner F.M., Bortolon A., Rosenthal A.M., Wilks T.M., Hughes J.W., Freeman C., Golfinopoulos T., Nagy A., Mauzey D. and Shafer M.W. (The DIII-D Team) 2021 *Rev. Sci. Instrum.* **92** 033522
[23] Summers H.P., Dickson W.J., O'Mullane M.G., Badnell N.R., Whiteford A.D., Brooks D.H., Lang J., Loch S.D. and Griffin D.C. 2006 *Plasma Phys. Control. Fusion* **48** 263–93
[24] Sciortino F. *et al* 2021 *Plasma Phys. Control. Fusion* **63** 112001
[25] Eldon D. *et al* 2012 *Rev. Sci. Instrum.* **83** 10E343
[26] Muscatello C.M. *et al* 2014 *Rev. Sci. Instrum.* **85** 11D702
[27] Van Zeeland M.A., Boivin R.L., Carlstrom T.N., Deterly T. and Finkenthal D.K. 2006 *Rev. Sci. Instrum.* **77** 10F325
[28] Chrystal C., Burrell K.H., Grierson B.A., Haskey S.R., Groebner R.J., Kaplan D.H. and Briesemeister A. 2016 *Rev. Sci. Instrum.* **87** 11E512
[29] Cardozo N.J.L. 1995 *Plasma Phys. Control. Fusion* **37** 799–852
[30] Dux R. 2006 STRAHL user manual *Technical Report*
[31] Naulin V. 2007 *J. Nucl. Mater.* **363-365** 24–31
[32] Naulin V., Garcia O.E., Nielsen A.H. and Rasmussen J.J. 2004 *Phys. Lett.* A **321** 355–65
[33] Savitzky A. and Golay M.J.E. 1964 *Anal. Chem.* **36** 1627–39
[34] Chilenski M.A., Greenwald M.J., Hubbard A.E., Hughes J.W., Lee J.P., Marzouk Y.M., Rice J.E. and White A.E. 2017 *Nucl. Fusion* **57** 126013
[35] Stangeby P.C. 1999 *The Plasma Boundary of Magnetic Fusion Devices* (CRC Press)
[36] Leonard A.W., McLean A.G., Makowski M.A. and Stangeby P.C. 2017 *Nucl. Fusion* **57** 086033
[37] Eich T. *et al* (ASDEX Upgrade Team and JET EFDA Contributors) 2013 *Nucl. Fusion* **53** 093031
[38] Stangeby P.C., Canik J.M., Elder J.D., Lasnier C.J., Leonard A.W., Eldon D., Makowski M.A., Osborne T.H. and Grierson B.A. 2015 *Nucl. Fusion* **55** 093014
[39] Haskey S.R. *et al* 2018 *Rev. Sci. Instrum.* **89** 10D110
[40] Sciortino F. 2021 Experimental inference of particle transport in tokamak plasmas Thesis Massachusetts Institute of Technology
[41] Sciortino F. *et al* 2022 *Plasma Phys. Control. Fusion* **64** 124002
[42] Meneghini O. *et al* (The AToM Team) 2015 *Nucl. Fusion* **55** 083008
[43] Pankin A., McCune D., Andre R., Bateman G. and Kritz A. 2004 *Comput. Phys. Commun.* **159** 157–84
[44] Van Zeeland M.A. and Carlstrom T.N. 2004 *Rev. Sci. Instrum.* **75** 3423–5
[45] Newville M., Stensitzki T., Allen D.B. and Ingargiola A. 2014 LMFIT: non-linear least-square minimization and curve-fitting for Python (available at: https://zenodo.org/record/11813)
[46] Newville M. et al 2021 lmfit/lmfit-py: 1.0.3 (available at: https://zenodo.org/record/5570790)
[47] Groth M. *et al* 2019 *Nucl. Mater. Energy* **19** 211–7
[48] Sontag A.C., Chen X., Canik J., Leonard A., Lore J.D., Moser A.L., Murakami M., Park J.M. and Petty C. 2017 *Nucl. Fusion* **57** 076025
[49] Sang C., Guo H., Stangeby P., Wang H., Wang L. and Wang D. 2020 *Nucl. Fusion* **60** 056011
[50] Whyte D.G. *et al* (the Alcator C-Mod Team) 2010 *Nucl. Fusion* **50** 105005
[51] Leonard A.W., Elder J.D., Canik J.M., Groebner R.J. and Osborne T.H. 2013 *J. Nucl. Mater.* **438** S246–9
[52] Horvath L. *et al* (JET Contributors) 2023 *Plasma Phys. Control. Fusion* **65** 044003
[53] Nelson A.O., Xing Z.A., Izacard O., Laggner F.M. and Kolemen E. 2021 *Nucl. Mater. Energy* **26** 100883
[54] Salmi A.T., Tala T.J.J., Bianchetti Morales R., Carvalho I. and Lomas P. 2023 *Plasma Phys. Control. Fusion* **65** 055025
[55] Chapman-Oplopoiou B. *et al* 2022 *Nucl. Fusion* **62** 086028
[56] Guttenfelder W., Groebner R.J., Canik J.M., Grierson B.A., Belli E.A. and Candy J. 2021 *Nucl. Fusion* **61** 056005